INL/EXT-21-XXX

M3 Milestone: Anisotropic Inelastic Deformation 2021

August 2021

Antonio Recuero, Daniel Schwen, and Sudipta Biswas

Idaho National Laboratory, Idaho Falls, ID 83415, USA

Changing the World's Energy Future

Idaho National Laboratory

INL/EXT-21-XXX

M3 Milestone: Anisotropic Inelastic Deformation 2021

Antonio Recuero, Daniel Schwen, and Sudipta Biswas

Idaho National Laboratory, Idaho Falls, ID 83415, USA

August 2021

Idaho National Laboratory
Computational Mechanics and Materials Department
Idaho Falls, Idaho 83415

http://www.inl.gov

Prepared for the
U.S. Department of Energy
Office of Nuclear Energy
Under DOE Idaho Operations Office
Contract DE-AC07-05ID14517

Page intentionally left blank

Contents

Page intentionally left blank

Milestone title

Add initial capability to handle anisotropic inelastic response for emerging fuel and cladding material models in BISON. Due 3/25/2021.

Milestone description

The focus on new fuel and cladding models are drivers for several new capabilities at the MOOSE and BISON levels. Since these materials are anisotropic, they require an extension of our inelastic mechanics capabilities, which currently heavily rely on radial return mapping and the assumption of isotropic stiffness. We plan to add additional code paths to support fully anisotropic materials without degrading the computational performance for modeling isotropic materials.

Completion criteria

Implement comprehensive support for anisotropic mechanical properties and document via a year-end report and in GitLab.

1 Introduction

The mechanical behavior of fuel cladding exhibits inelastic anisotropic behavior. An example of this is the texture introduced in Zircaloy-4 by the cold rolling manufacturing process—a texture that cannot be fully eliminated by an ensuing annealing heat treatment [9]. The low-symmetry properties of hexagonal close-packed Zircaloy grains cause permanent deformation that is influenced by the orientation (or texture) of crystal grains.

The complex microscopic reality of cladding materials gives rise to a variety of mechanical and behavioral classifications. Broadly speaking, emerging fuel and cladding cladding materials respond differently depending on the local material's directions or, in other words, they exhibit anisotropy. Cladding material's elastic behavior can be described by considering anisotropy in the elasticity tensor definition [12]. A subset of directionally-dependent behavior with permanent deformation can be characterized by Hill's plasticity, with the material's yield function being described by a generalization of von Mises plasticity. Further, materials can experience anisotropic behavior while yielding or creeping. When this inelastic deformation is plastic, the combined isotropic elastic and anisotropic plastic behavior is usually referred to as "anisotropic plasticity." If the elastic behavior is also directionally dependent, its behavior can be called "anisotropic elasto-plasticity." Hill's yield criterion and some of its extensions can also be employed to model creep compliance in cladding materials (see [8])

In this work, we extend inelastic deformation in MOOSE to include the consideration of anisotropy, enabling a framework that can be leveraged by high-fidelity BISON numerical experiments. The implementation adds its own class hierarchy and therefore does not degrade the performance of existing creep and plasticity models in the Tensor Mechanics module or in BISON. The engineering-scale implementation allows for the potential integration of surrogate models capturing microstructure evolution. Therefore, the current work can be extended to drive the inelastic deformation by mechanistically-informed reduced-order models, as recently accomplished in MOOSE for isotropic materials [22].

2 Activities

This milestone focuses on enabling the simulation of general anisotropic materials using Hill-like yield criteria. This work includes the following items:

- **Elastic anisotropy**. Anisotropic elasticity tensors are now rotated to accommodate the incremental kinematics used in MOOSE. Initial verification was performed.
- **Literature review**. A literature review was performed to evaluate the state of the art of anisotropic plasticity algorithms and typical anisotropy modeling approaches. This work focused on two relevant aspects. On one hand, the way anisotropy is modeled for typical clad materials was surveyed. Hill's plasticity was found to be a typical choice in this regard [4, 21]. More adaptive and asymmetric anisotropic yield surfaces for hexagonal close-packed metals exist (see [1]). As a second step, a couple of algorithmic options were analyzed. The improved return mapping behavior of Ref. [23] was found to provide potential benefits in terms of iteration stability, as its convergence rate is superior to those of closest-point projection (CPP) approaches. These latter approaches, however, carry the potential to solve general anisotropic equations (see [11, 17] for a performance analysis of various CPP approaches).
- **Generalized return mapping framework**. A hierarchy of classes to address the return mapping for anisotropic materials was designed and created. This hierarchy is very similar to the pre-existing isotropic one, since iterations occur on a single variable. However, the new hierarchy offers flexibility when passing deviatoric and full Cauchy stress tensors, and enables simplification of the return mapping fallback options.
- **Hill's creep**. A Hill-like [5] yield function for creep was implemented in conjunction with a temperature-dependent power law
(class name: "`ADHillCreepStressUpdate`"). This class can easily be expanded to address the more accurate physical approaches available in BISON in order to include, for example, thermal or irradiation dose dependencies.
- **Hill's plasticity**. Hill's plasticity with isotropic elastic behavior was implemented in the class "`ADHillPlasticityStressUpdate`". Initial verification was performed.
- **Anisotropic elastoplasticity**. Hill's plasticity with anisotropic elastic behavior was implemented in the class
"`ADHillElastoPlasticityStressUpdate`". Verification is limited for this class.
- **Transformation of Hill's tensor**. The transformation of the Hill's tensor to capture simulation scenarios in which global axes are not aligned with material anisotropy axes was implemented (e.g. to address large deformation kinematics and rigid body motion). The transformed Hill's tensor can be used for modeling anisotropic creep, anisotropic plasticity, and combined anisotropic creep-plasticity.
- **Creep numerical integration error** The influence of the time step on the accuracy of the creep solution was investigated. An additional time step criterion, which is function of the material point's stress increment, was added as an option to the user.

- **Application in BISON** The anisotropic creep implementation has been applied to a number of loss-of-coolant-accident (LOCA) simulation scenarios in BISON in conjunction with advanced Zircaloy thermal creep models. Further investigation is needed to better leveraging experimental data capturing material's anisotropy.

3 MOOSE implementation for Hill's plasticity

This section outlines the foundation of the equations and algorithms implemented in MOOSE to simulate anisotropic metals. A framework for Hill-like creep/plasticity that iterates on a scalar plastic multiplier, as presented in detail in the work by Versino and Bennett [23], was implemented with generality in the Tensor Mechanics module.

3.1 Background

We can write the yield function of a Hill material as follows:

$$f_y = \frac{1}{2}\boldsymbol{\sigma}^T \boldsymbol{A}\boldsymbol{\sigma} - \sigma_y^2(\alpha, \beta) \leq 0, \tag{1}$$

where f_y is a yield function, $\boldsymbol{\sigma}$ is the Cauchy stress tensor in Voigt form, α is an isotropic hardening variable that captures the amount of plastic excursion, and β is a generic parameter or variable influencing the hardening function σ_y. The 6×6 Hill's tensor $\boldsymbol{A}$ modifies the von-Mises yield criterion in order to describe anisotropic plastic deformation. $\boldsymbol{A}$, when local material axes are trivially aligned with global axes, can be written as follows:

$$\boldsymbol{A} = \begin{bmatrix} G+H & -H & -G & 0 & 0 & 0 \\ -H & F+H & -F & 0 & 0 & 0 \\ -G & -F & F+G & 0 & 0 & 0 \\ 0 & 0 & 0 & 2N & 0 & 0 \\ 0 & 0 & 0 & 0 & 2L & 0 \\ 0 & 0 & 0 & 0 & 0 & 2M \end{bmatrix}. \tag{2}$$

In scalar form, the Hill's yield criterion may be expressed as:

$$\Phi_{\text{Hill}} = F(\sigma_{22}-\sigma_{33})^2 + G(\sigma_{33}-\sigma_{11})^2 + H(\sigma_{11}-\sigma_{22})^2 + 2L\sigma_{23}^2 + 2M\sigma_{31}^2 + 2N\sigma_{12}^2. \tag{3}$$

The constants F, G, H, L, M, and N are experimentally determined to capture the anisotropy of the yield surface. In particular, the normal $(\sigma_1^y, \sigma_2^y, \sigma_3^y)$ and shear $(\tau_{12}^y, \tau_{23}^y, \tau_{31}^y)$ yield stresses depend on the axes of anisotropy. Using this assumed prior knowledge, the Hill's constants can be determined:

$$\begin{aligned} F &= \frac{\tilde{\sigma}^2}{2}\left[\frac{1}{(\sigma_{22}^y)^2} + \frac{1}{(\sigma_{33}^y)^2} - \frac{1}{(\sigma_{11}^y)^2}\right], \\ G &= \frac{\tilde{\sigma}^2}{2}\left[\frac{1}{(\sigma_{33}^y)^2} + \frac{1}{(\sigma_{11}^y)^2} - \frac{1}{(\sigma_{22}^y)^2}\right], \\ H &= \frac{\tilde{\sigma}^2}{2}\left[\frac{1}{(\sigma_{11}^y)^2} + \frac{1}{(\sigma_{22}^y)^2} - \frac{1}{(\sigma_{33}^y)^2}\right], \\ L = \frac{\tilde{\sigma}^2}{2}\left[\frac{1}{(\tau_{23}^y)^2}\right],\ M &= \frac{\tilde{\sigma}^2}{2}\left[\frac{1}{(\tau_{31}^y)^2}\right],\ \text{and } N = \frac{\tilde{\sigma}^2}{2}\left[\frac{1}{(\tau_{12}^y)^2}\right], \end{aligned} \tag{4}$$

where $\tilde{\sigma}$ denotes a reference yield stress. The parameter choice $F = G = H = 0.5$ corresponds to isotropic axial behavior.

3.2 Anisotropic plasticity algorithm

Fundamentally, isotropic plasticity in MOOSE is implemented through algorithms reported in monographs (see [3, 18]). The extension of these algorithms to anisotropic plasticity was carried out by drawing on a recent research work [23]. The algorithms therein perform a "generalized" radial-return (GRR) via an algorithm that accommodates plastic and elastoplastic anisotropy. These algorithms utilize eigendecomposition of the anisotropy tensor, $\boldsymbol{A}$, and anisotropic elasticity tensor, $\boldsymbol{C}$. In addition, the diagonalization of some matrices involved in the generalized return mapping computations allows for expressing the update of the stress vector (after a successful return to the yield surface) as a function of an easily invertible diagonal matrix.

Despite the GRR anisotropic algorithms possibly exhibiting a higher computational effort per integration point, they show potential for making general simulations more robust, due to their high convergence rates. The generalized return mapping algorithm shows improved performance over the closest-point projection approach. In fact, the GRR algorithm can return to the yield surface in few iterations even when the initial guess is far from the solution. On the other hand, elastoplastic anisotropy requires the computation of eigendecompositions of 6×6 matrices and the solution of a linear 6×6 system of equations. This step can become computationally demanding for problems in which an anisotropic elasticity tensor changes both over time and spatially (e.g., due to thermal effects). Additionally, generalization of the classical return mapping imposes some restrictions on the shape of the yield surface, thereby limiting its applicability to von Mises like plasticity.

The GRR approach was selected to ensure the minimum solver robustness that we expect will enable application of anisotropic plasticity to advanced simulations in BISON. The favorable convergence rates of GRR are expected to overcome some of the convergence issues in the Gauss point-level yield surface return iterations—issues frequently alleviated by linear search and substepping procedures (i.e., subdividing the system time step to achieve local convergence, at the expense of increasing the computational effort).

3.3 Class design and documentation in MOOSE

To avoid interfering with the already-complex implementation of the isotropic radial-return mapping classes, the inelastic anisotropy implementation creates an additional hierarchy of classes. This design decision prevents any performance degradation in the existing classes. As a result, a new set of material classes in the Tensor Mechanics module was added (see Fig. 1 for an inheritance diagram). This hierarchy is, of course, easily expandable to consider other plastic hardening laws, creep equations, etc. The design accounts for the possible combination of anisotropic creep and plasticity in a single material block, which is managed by the `ADComputeMultipleInelasticStress` object.

Markdown documentation on the three mechanical applications offers a brief explanation on the class, relevant references, input file examples, and user choices. The documentation shown in Fig. 2 will be expanded with future changes.

The new set of classes that allows the generalized return-mapping algorithm to contribute to the system's residual is analogous to existing isotropic plasticity classes. Excerpt 3.3 shows the required input for computing the solution to an anisotropic plastic problem. Tolerances of the return mapping can be selected to be almost machine precision. The simulation's time step can be

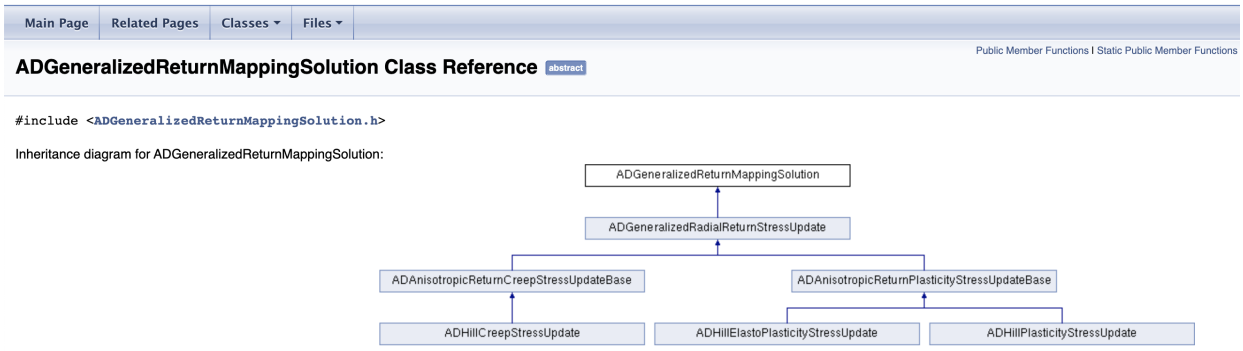

Figure 1: New C++ class hierarchy depicted in Doxygen documentation.

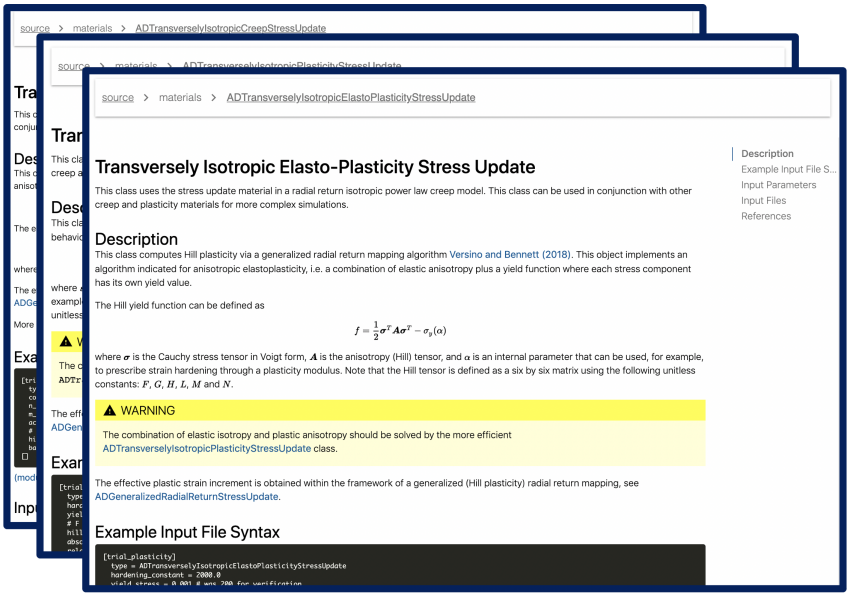

Figure 2: MOOSE's markdown documentation of anisotropy classes.

limited by a measure of the inelastic strain in order to avoid taking large steps that would compromise simulation accuracy. This feature is available in all anisotropy classes through the "material time step" control. Currently, automatic differentiation classes are available for anisotropic creep, plasticity, and elastoplasticity. These classes must be used in conjunction with the existing class `ADComputeMultipleInelasticStress`.

```
[trial_plasticity]
  type = ADHillPlasticityStressUpdate
  hardening_constant = 200.0
  yield_stress = 200.0
  absolute_tolerance = 1e-14
  max_inelastic_increment = 2.0e-6
  internal_solve_output_on = on_error
[]
```

4 Initial numerical results and verification

4.1 Hill's plasticity

Here, we present initial verification of anisotropic plasticity via a simple uniaxial bar problem. Symmetric Dirichlet boundary conditions are used at one end; on the other, a uniform normal pressure that linearly increases with time is applied. An image of the three-dimensional mesh during the simulation is shown in Fig. 3.

The elastic regime of this bar is characterized by isotropic constants: a Young's modulus of 70 GPa and a Poisson's ratio of 0.25. The flow stress is defined here as $\sigma_y = \sigma_{y0} + H\alpha$, with the yield stress being $\sigma_{y0} = 200$ MPa, the hardening slope being $H = 200$ MPa, and α being an internal variable capturing isotropic hardening. The anisotropy of the plastic yield surface is defined by the following Hill's constants: $F = 0.58298$, $G = 0.36442$, $H = 0.63422$, $L = 2.06914$, $M = 2.34923$, and $N = 1.81459$. With these values, assuming the bar is oriented along one global coordinate axis, we can predict the axial strain value at which the bar will enter an irreversible deformation stage. Onset of plastic behavior, according to Eq. 1, depends on the loading direction.

If the bar is oriented along the global x-axis, the following equation defines the beginning of yielding:

$$\sigma_{y0} = \sqrt{\left(\frac{1}{2}(G+H)\sigma_{11}\right)} \rightarrow \sigma_{11} = 283.03\text{MPa}. \tag{5}$$

Similarly, if the bar is loaded longitudinally, along the y-direction:

$$\sigma_{y0} = \sqrt{\left(\frac{1}{2}(F+H)\sigma_{22}\right)} \rightarrow \sigma_{22} = 256.36\text{MPa}. \tag{6}$$

Figure 4 shows the numerical results from running this simple verification problem in MOOSE. The yield stress values match the theoretical results at up to four significant digits. For this problem, the vast majority of the return mapping calls achieved numerical errors close to machine precision within two to three iterations. In addition, the same problem was run through the `ADHillElastoPlasticityStressUpdate` class, which incorporates the more complex algorithmic basis for anisotropic elastoplasticity. This latter case also retrieved the reference solution.

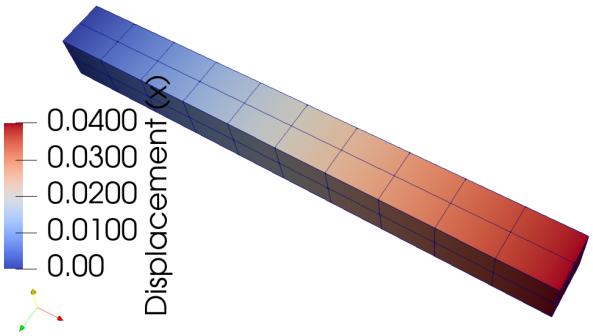

Figure 3: Uniaxial bar problem subjected to an axial load. Material points in the bar evolve from the elastic to the plastic regime, where the yield function is defined by Hill's constants.

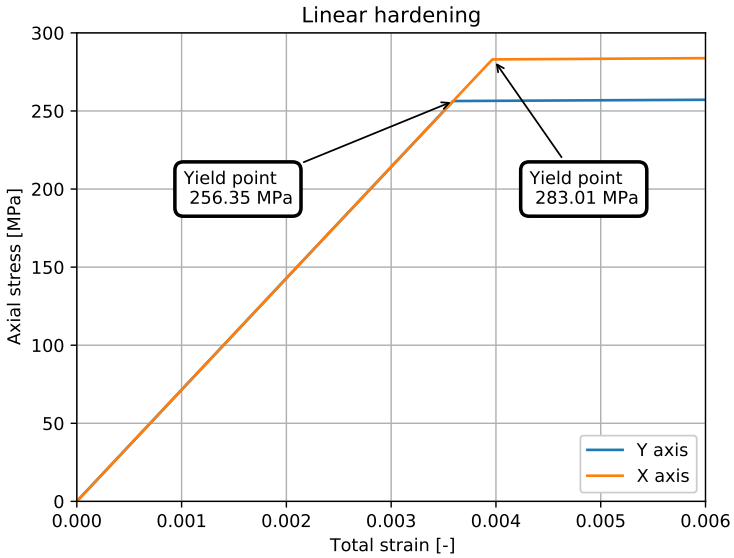

Figure 4: Three-dimensional bar total uniaxial strain at two orientations. Analytical prediction of yield points is provided via Eqs. 5 and 6.

4.2 Hill's creep

Material creep can be described by Hill's parameters (in a manner analogous to Hill's yield surface) via the coefficients F, G, H, L, M, and N. An equivalent Hill's stress may be defined as:

$$q(\boldsymbol{\sigma}) = \big(\big[F(\sigma_{22}-\sigma_{33})^2 + G(\sigma_{33}-\sigma_{11})^2 + H(\sigma_{11}-\sigma_{22})^2 \\ +2L\tau_{23}^2 + 2M\tau_{13}^2 + 2N\tau_{12}^2\big]\big)^{\frac{1}{2}}, \tag{7}$$

where it is assumed that the material's directions are aligned with global axes. $q(\boldsymbol{\sigma})$ denotes a function that determines an equivalent stress through weighting of its components. Using a simple power law, the creep strain rate can be determined as:

$$\dot{\epsilon}_c = A_{pl} q(\boldsymbol{\sigma})^n t^m, \tag{8}$$

where A_{pl} is the power law coefficient, n and m are model exponent parameters, and t is the simulation time. Initial verification of uniaxial creep was performed along the three spatial directions: x, y, and z. The setup and mesh are identical to those shown in Fig. 3. As with the previous test case, the elastic behavior is characterized by isotropic constants: a Young modulus of 700 MPa and a Poisson's ratio of 0.0. Uniform pressure stretches the bar from zero to 40 MPa linearly during the period from $t = 0\,\text{s}$ to $t = 0.001\,\text{s}$; after that, the load is constant while the bar creeps. The creep model parameters are as follows: $n = 9$, $m = 0$, and $A_{pl} = 10^{-16}$. The Hill's creep coefficients for this case were selected to be $F = 0.5$, $G = 0.25$, and $H = 0.3866$. Equation 8 allows for computing the creep strain rate along various directions. In particular, we can infer that the creep strain (and its rate) must fulfill the following relationships:

$$\dot{\epsilon}_{cx} \propto (\sqrt{(G+H)})^{n+1},\ \dot{\epsilon}_{cy} \propto (\sqrt{(F+H)})^{n+1},\ \dot{\epsilon}_{cz} \propto (\sqrt{(F+G)})^{n+1}. \tag{9}$$

Furthermore, the simulation outcomes yield the following results at the final time step: $\epsilon_{cx}^{sim} = 2.7407 \cdot 10^{-6}$, $\epsilon_{cy}^{sim} = 1.4360 \cdot 10^{-5}$, and $\epsilon_{cz}^{sim} = 6.2205 \cdot 10^{-6}$.

Theoretical ratios can be compared against numerical results. These analytical ratios and their corresponding numerical results are satisfactory up to four significant digits (see Eq. 10).

$$\begin{aligned} \frac{\dot{\epsilon}_{cx}}{\dot{\epsilon}_{cy}} &= 0.1909 \simeq \frac{\dot{\epsilon}_{cx}^{sim}}{\dot{\epsilon}_{cy}^{sim}} = 0.1909, \\ \frac{\dot{\epsilon}_{cx}}{\dot{\epsilon}_{cz}} &= 0.4406 \simeq \frac{\dot{\epsilon}_{cx}^{sim}}{\dot{\epsilon}_{cz}^{sim}} = 0.4406, \quad \text{and} \\ \frac{\dot{\epsilon}_{cy}}{\dot{\epsilon}_{cz}} &= 2.3085 \simeq \frac{\dot{\epsilon}_{cy}^{sim}}{\dot{\epsilon}_{cz}^{sim}} = 2.3085. \end{aligned} \tag{10}$$

Another way of verifying the implementation is based on the time integration of Eq. 8, using our model's parameters: $\epsilon_c = A_{pl} q(\tilde{\sigma})^n t_{end}$. By substituting the values for each direction and the final simulation time, $t_{end} = 0.001\,\text{s}$, we arrive at the following longitudinal creep strain values for the three orientations: $\epsilon_{cx}^{pl} = 2.7408 \cdot 10^{-6}$, $\epsilon_{cy}^{pl} = 1.4361 \cdot 10^{-5}$, and $\epsilon_{cz}^{pl} = 6.2208 \cdot 10^{-6}$. The final results are $\epsilon_{cx}^{sim} = 2.7402 \cdot 10^{-6}$, $\epsilon_{cy}^{sim} = 1.4360 \cdot 10^{-5}$, and $\epsilon_{cz}^{sim} = 6.2205 \cdot 10^{-6}$. The small discrepancies can be attributed to creep strain rate numerical integration error and time step selection.

Versions of these tests were added to the MOOSE repository as regression tests to ensure the stability of the implementation.

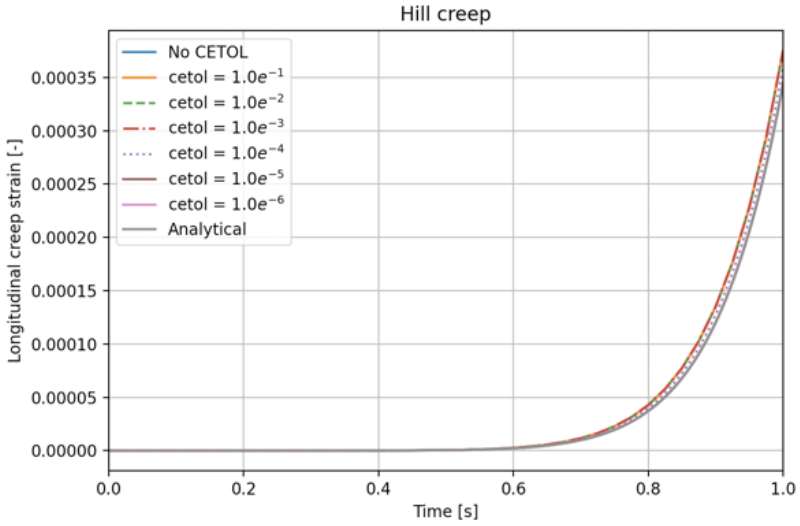

Figure 5: Uniaxial bar simulation with various user specified creep numerical integration error tolerance values.

5 Anisotropic material and implementation features

A number of code features were added to enable the practical use of these set of inelastic anisotropic classes by analysts.

5.1 Creep numerical integration

The radial return algorithm used to compute creep strain increments relies on the additive decomposition of elastic and inelastic strains. Using a one-dimensional problem as an example, the stress increment is given by $\Delta\sigma = E\Delta\varepsilon^{\text{elastic}} = E(\Delta\varepsilon^{\text{total}} - \Delta\varepsilon^{\text{creep}})$, where E represents the Young modulus. One expects that the error in the numerical integration of creep to be significantly less that the total strain increment, i.e. $err_{\text{creep}} \ll \frac{\Delta\sigma}{E}$. If we estimate the upper bound of error incurred as $err_{\text{creep}} = (\dot{\varepsilon}_{t+\Delta t} - \dot{\varepsilon}_t) \cdot \Delta t$, we can estimate the time step limit due to the numerical integration of creep as

$$\Delta t_{\text{limit}} = \frac{\Delta t \cdot E}{\Delta\sigma} \text{creep\_tolerance}. \tag{11}$$

An example on the use of the this time step limiter is given in Figs. 5 and 6 for a uniaxial bar, where various values of creep tolerances are used in the input file together with a "soft" terminator[1]. As the creep tolerance ("cetol" in the figures) prescribed decreases, moose's numerical results converge toward the analytical results.

Use of this additional creep numerical integration error tolerance parameter, which can be set using the `max_integration_error` MOOSE input parameter, is recommended.

5.2 Temperature dependency

A `HillConstant` MOOSE material was created to handle updates to the Hill's tensor (see Eq. 2) due to temperature, initial rigid body orientation, and rotation due to finite strain kinematics. Metal

[1] A "soft" terminator will render a current step failed if the current material time step is smaller than the current time step.

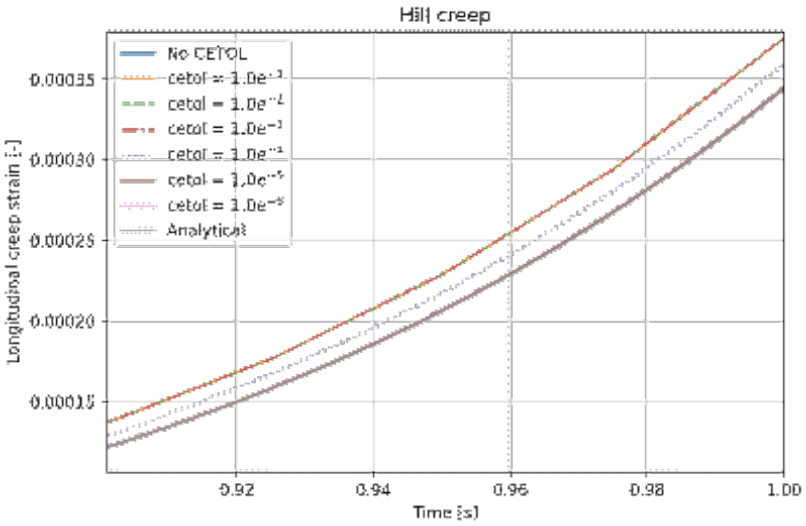

Figure 6: Uniaxial bar simulation with various creep numerical integration error values (zoomed-in). As the prescribed error tolerance becomes smaller the numerical results converge with the analytical solution.

anisotropy, typically introduced by manufacturing processes, can evolve with temperature. Experimental data for Hill's anisotropy coefficients of cladding materials can be obtained from the literature, see, e.g., [2], which allow to incorporate the effects of texture evolution into a thermo-mechanical simulation.

The user can provide functions of the coefficients F, G, H, L, M, and N with temperature to capture texture evolution during the simulation.

5.3 Large strain kinematics

In addition to temperature evolution, when structural components undergo large deformation (or rigid body rotation), the directions of anisotropy change. These nonlinear effects have been incorporated into the `HillConstant` material, which performs the following transformation:

$$\boldsymbol{A}^{\text{tr}} = \boldsymbol{T}\boldsymbol{A}\boldsymbol{T}^{T}, \tag{12}$$

where $\boldsymbol{T}$ is a 6×6 transformation tensor that is used to transform Hill's compliance tensor, and $\boldsymbol{A}$ and $\boldsymbol{A}^{\text{tr}}$ are the untransformed and transformed Hill's compliance tensor, respectively. Hill's equivalent quantities (see, e.g., Eq. 3) can also be obtained and generalized in tensor form [19]. A set of verification tests that ensure the transformation of the Hill's tensor is computed properly was added to the MOOSE repository.

5.4 Input file example

Typical input file sections for creep looks as follows

```
[hill_constants_material]
  type = HillConstants
  # F G H L M N
  hill_constants = "0.6 0.4 0.5 1.5 1.5 1.5"
```

```
  function_names = 'F G H L M N'
  temperature = temperature
[]
[anisotropic_creep]
  type = ADHillCreepStressUpdate
  coefficient = 1e-16
  n_exponent = 9
  m_exponent = 0
  activation_energy = 0
  max_inelastic_increment = 0.00003
  relative_tolerance = 1e-14
  absolute_tolerance = 1e-14
  max_integration_error = 1.0e-5
[]
```

where `function_names` refers to MOOSE functions defining the evolution of the Hill's coefficients, `temperature` refers to the name of the simulation's temperature variable, and `max_integration_error` allows the user to limit the creep strain time integration error.

6 Application to loss-of-coolant accidents

In this section, anisotropic creep is applied to various BISON assessment cases. Specifically, we employ the setup used to validate the cladding burst modeling against experimental data and use sets of anisotropic coefficients taken from the literature for numerical comparison.

Here we present three sets of numerical parameters: (1) the original, validated BISON results based on an accurate isotropic creep model: `ZryCreepLOCAErbacherLimbackHoppeUpdate`; (2) the thermal creep model (1) with anisotropic paramters that account for temperature evolution (α and β phases influence on anisotropy); and (3), same as (2) but with constant Hill's tensor coefficients. For the anisotropic creep runs, the Hill's compliance tensor is transformed according to large strain kinematics rotation. Parameters for (1) uses default existing values. The simulation with parameters (2) considers the evolution of anisotropy for the two phases of Zircaloy-4: $F = 0.738$, $G = 0.588$, and $H = 0.174$ at room temperature, and $F = 0.570$, $G = 0.480$, and $H = 0.450$ at 1073 K[2] [16]. The simulation with parameter set (3) assumes anisotropy to be independent of temperature; the parameters are taken from [7]: $F = 0.956$, $G = 0.304$ and $H = 0.240$.

Since no calibration of parameters was performed in this study (the anisotropic coefficients are taken from the literature for given thermally treated Zircaloy-4), the results presented in this section do not represent any form of validation but a measure of the influence of creep anisotropy on various LOCA modeling scenarios. The originally isotropic Erbacher-Limback-Hoppe creep model is here numerically modified to account for creep anisotropy.

6.1 ORNL Zircaloy-4

These Zircaloy-4 burst tests were performed by Oak Ridge National Laboratory [10]. Key metrics for simulating this test are the time evolution of hoop stresses and strains. The outwards deformation of the cladding increases rapidly due to thermal creep as the temperature rises. The ensuing

[2]Note that due to the the axisymmetric problem's variable convention in MOOSE, and the orientation of the pin in the global frame, the order of these constants were modified in the input file (G and H values need to be swapped).

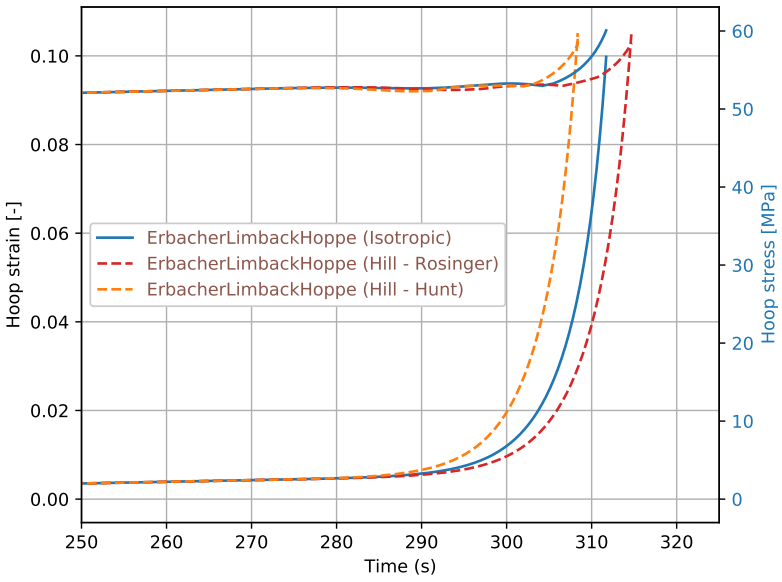

Figure 7: Evolution of hoop strains and stresses during the numerical experiment (ORNL-Zr4).

high levels of clad deformation may result in rapid development of burst phenomena. A relevant outcome of the validation process is BISON's mere 2% error in predicting the time to burst.

Figure 7 shows the evolution of the hoop strains and stresses for three sets of creep parameters. The isotropic simulation burst takes place at 311.7 s (1056 K), the use of temperature-dependent anisotropy (Rosinger) generates cladding failure at 314.7 s (1072 K), and constant anisotropic coefficients (Hunt) predict bursting at 308.3 s (1038 K). This is consistent with research works which highlight that the texture of the various phases of Zircaloy can have a moderate influence on the burst temperature and burst strains [15, 20]. The results obtained here for this type of experiments are consistent in terms of burst time variability [2].

6.2 REBEKA 10MPa - Zircaloy-4

A similar numerical experiment is carried out for a REBEKA case at 10 MPa of internal pressure. The results are shown in Fig. 8. The original isotropic BISON results underpredicts the burst temperature (predicted: 989 K, experiment: 1010 K) and makes cladding burst 416.2 s into the simulation. Use of Rosinger's anisotropy coefficient pushes the burst temperature in the right direction (1012.1 K) and simulation's burst time is predicted at 439.0 s. Finally, use of Hunt's anisotropy coefficients further underpredicts the burst temperature (984 K).

6.3 PUZRY-20 Zircaloy-4

Similarly to the previous two LOCA cases, anisotropic creep is applied to one case of the PUZRY test series (PUZRY-20), see [6, 14]. The experimental results predict burst pressure at 2.722 MPa and burst time at 2211.1 s. The validated isotropic results are at 2.64 MPa and 2173 s; Hunt's data yield 2.83 MPa and 2215.8 s, and Rosinger's phase-dependent coefficients yield 3.17 MPa and 2367.1 s.

In general, the consideration of Zircaloy-4 creep anisotropy increases the hoop strains at burst time.

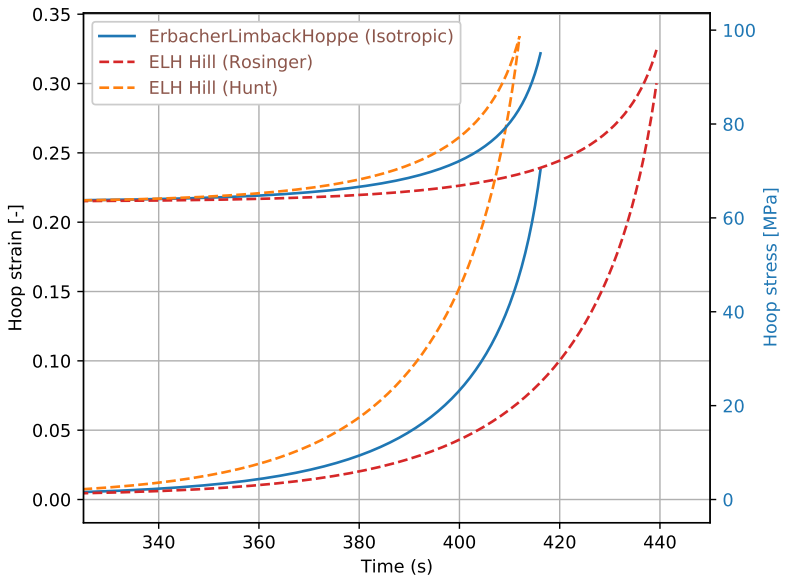

Figure 8: Evolution of hoop strains and stresses during the numerical experiment (rebeka-10).

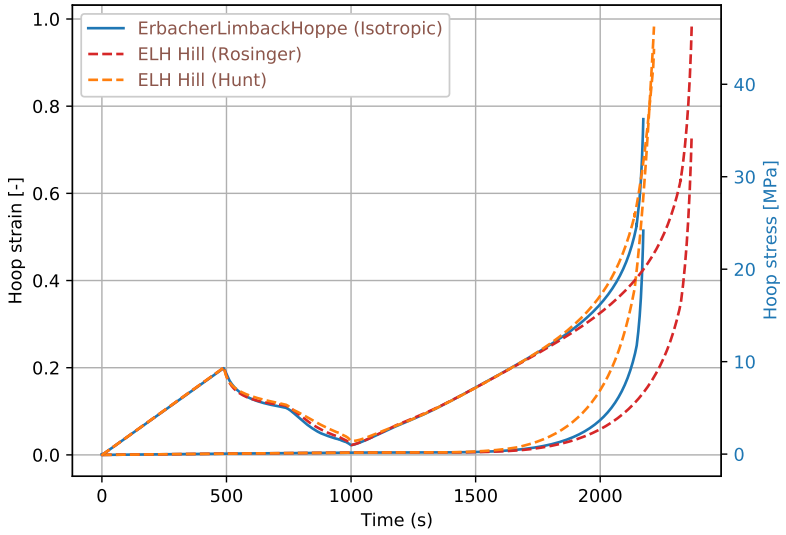

Figure 9: Evolution of hoop strains and stresses during the numerical experiment (puzry-20).

7 Conclusions

This document summarizes the implementation and verification of anisotropic creep and plasticity in MOOSE and its application to advance fuel creep models in loss of coolant accident simulations. The anisotropic inelastic deformation framework developed here can be leveraged to more accurately consider directional inelastic deformation in materials. Use of calibrated parameters and further study on the validation of anisotropic inelastic models in nuclear fuel scenarios remain as future work.

Anisotropic creep and plasticity can additionally be informed by reduced-order models capturing the material's microstructure state evolution. This can be accomplished by using the new class hierarchy similarly to how it was carried out for isotropic materials. Finally, more general inelastic anisotropy formulations beyond van Mises like formulations can be implemented by making use of, e.g., the closest point projection algorithm [13]. This item remains as future work.

References

[1] Cazacu, O., Plunkett, B., and Barlat, F. (2006). Orthotropic yield criterion for hexagonal closed packed metals. *International Journal of Plasticity*, 22(7):1171–1194.

[2] Choi, G.-H., Shin, C.-H., Kim, J. Y., and Kim, B. J. (2021). Circumferential steady-state creep test and analysis of zircaloy-4 fuel cladding. *Nuclear Engineering and Technology*.

[3] Dunne, F. and Petrinic, N. (2005). *Introduction to Computational Plasticity*. Oxford University Press on Demand.

[4] Godavarti, P. S., Hussien, S., and Murty, K. L. (1988). Effect of annealing temperature on yield anisotropy of Zircaloy-4 Trex. *Metallurgical Transactions A*, 19(5):1243–1255.

[5] Hill, R. (1950). *The Mathematical Theory of Plasticity*. Oxford engineering science series. Clarendon Press.

[6] Hózer, Z., Perez-Feró, E., Győri, C., Matus, L., Vasáros, L., Windberg, P., Maróti, L., Horváth, M., Nagy, I., Pintér-Csordás, A., et al. (2007). Experimental database of e110 claddings under accident conditions aeki-frl-2007-123-01/01, nea-1799 ifpe/aeki-edb-e110.

[7] Hunt, C. (1975). Anisotropic theory and the measurement and use of the anisotropic factors for zircaloy-4 fuel sheaths.

[8] Linga Murty, K. and Charit, I. (2006). Texture development and anisotropic deformation of zircaloys. *Progress in Nuclear Energy*, 48(4):325–359.

[9] Liu, C., Li, G., Chu, L., Gu, H., Yuan, F., Han, F., and Zhang, Y. (2018). Texture and yielding anisotropy of Zircaloy-4 alloy cladding tube produced by cold pilger rolling and annealing. *Materials Science and Engineering: A*, 719:147–154.

[10] Massey, C. P., Terrani, K. A., Dryepondt, S. N., and Pint, B. A. (2016). Cladding burst behavior of fe-based alloys under LOCA. *Journal of Nuclear Materials*, 470:128–138.

[11] Miñano, M., Caminero, M. A., and Montáns, F. J. (2016). On the numerical implementation of the closest point projection algorithm in anisotropic elasto-plasticity with nonlinear mixed hardening. *Finite Elements in Analysis and Design*, 121:1–17.

[12] Nakatsuka, M. (1981). Elastic anisotropy of zirconium alloy fuel cladding. *Nuclear Engineering and Design*, 65(1):103–112.

[13] Ortiz, M., Pinsky, P. M., and Taylor, R. L. (1983). Operator split methods for the numerical solution of the elastoplastic dynamic problem. *Computer Methods in Applied Mechanics and Engineering*, 39(2):137–157.

[14] Perez-Feró, E., Hózer, Z., Novotny, T., Kracz, G., Horváth, M., Nagy, I., Vimi, A., Pintér-Csordás, A., Győri, C., Matus, L., Vasáros, L., Windberg, P., and Maróti, L. (2013). Experimental Database of E110 Claddings under Accident Conditions. Technical Report EK-FRL-2012-255-01/02, Centre for Energy Research, Hungarian Academy of Sciences, Budapest, Hungary.

[15] Rosinger, H. E. (1984). A model to predict the failure of Zircaloy-4 fuel sheathing during postulated LOCA conditions. *Journal of Nuclear Materials*, 120(1):41–54.

[16] Rosinger, H. E., Bowden, J., and Shewfelt, R. S. W. (1982). The anisotropic creep behaviour of Zircaloy-4 fuel cladding at 1073 K. Technical report, Atomic Energy of Canada Ltd., Pinawa, Manitoba, Whiteshell Nuclear Research Establishment.

[17] Scherzinger, W. M. (2017). A return mapping algorithm for isotropic and anisotropic plasticity models using a line search method. *Computer Methods in Applied Mechanics and Engineering*, 317:526–553.

[18] Simo, J. C. and Hughes, T. J. R. (2006). *Computational inelasticity*, volume 7. Springer Science & Business Media.

[19] Stewart, C. M., Gordon, A. P., Ma, Y. W., and Neu, R. W. (2011). An anisotropic tertiary creep damage constitutive model for anisotropic materials. *International Journal of Pressure Vessels and Piping*, 88(8-9):356–364.

[20] Suman, S. (2019). Burst criterion for indian PHWR fuel cladding under simulated loss-of-coolant accident. *Nuclear Engineering and Technology*, 51(6):1525–1531.

[21] Takuda, H., Yoshii, T., and Hatta, N. (1999). Finite-element analysis of the formability of a magnesium-based alloy az31 sheet. *Journal of Materials Processing Technology*, 89:135–140.

[22] Tallman, A. E., Arul Kumar, M., Matthews, C., , and Capolungo, L. (2021). Surrogate modeling of viscoplasticity in steels: Application to thermal, irradiation creep and transient loading in HT-9 cladding. *JOM*, 73:126–137.

[23] Versino, D. and Bennett, K. C. (2018). Generalized radial-return mapping algorithm for anisotropic von mises plasticity framed in material eigenspace. *International Journal for Numerical Methods in Engineering*, 116(3):202–222.